Ground-state order in magic-angle graphene at filling $\nu = -3$: A full-scale density matrix renormalization group study

Tianle Wang,[1,2] Daniel E. Parker,[3] Tomohiro Soejima (副島智大),[1] Johannes Hauschild,[4] Sajant Anand,[1] Nick Bultinck,[5,6] and Michael P. Zaletel[1,2]

[1]*Department of Physics, University of California, Berkeley, California 94720, USA*
[2]*Materials Science Division, Lawrence Berkeley National Laboratory, Berkeley, California 94720, USA*
[3]*Department of Physics, Harvard University, Cambridge, Massachusetts 02139, USA*
[4]*Department of Physics, Technische Universität München, 85748 Garching, Germany*
[5]*Rudolf Peierls Centre for Theoretical Physics, University of Oxford, Oxford OX1 3PU, United Kingdom*
[6]*Department of Physics, Ghent University, 9000 Ghent, Belgium*

(Received 28 November 2022; revised 28 September 2023; accepted 5 October 2023; published 8 December 2023)

We investigate twisted bilayer graphene (TBG) at filling $\nu = -3$ in the presence of realistic heterostrain. Strain amplifies the band dispersion and drives the system beyond the strong-coupling regime of previous theoretical studies. We use DMRG to conduct an unbiased, large-scale numerical calculations that include all spin and valley degrees of freedom, up to bond dimension $\chi = 24\,576$. We establish a global phase diagram that unifies a number of theoretical and experimental results. Near zero strain we find an intervalley-coherent quantized anomalous Hall (QAH-IVC) state, a competitive strong-coupling order that evaded past numerical studies. A tiny strain around 0.05% drives a transition into an incommensurate Kekulé spiral (IKS) phase, supporting the mean-field prediction in [Kwan *et al.*, Phys. Rev. X **11**, 041063 (2021)]. Even higher strains above 0.2% favor a flavor-symmetric metallic order, which may explain metals found at $\nu = -3$ in many experiments.

DOI: 10.1103/PhysRevB.108.235128

In recent years, the nature of strongly correlated states in magic-angle twisted bilayer graphene (TBG), in particular at integer fillings $\nu \in (-4, +4)$, has been the center of experimental investigations. However, consensus on the ground state order has still not been achieved. Comparing numerous experimental reports [1–14] (see also Appendix A in the Supplemental Material [15]) reveals a persistent puzzle: Although these reports reach consensus at all even fillings $\nu = 0, \pm 2$ and one odd filling $\nu = +3$, all identified as correlated insulators, results at other fillings remain inconsistent. This is particularly acute at filling $\nu = -3$, where metals, insulators, and even superconductors have all been observed. Such a rich phenomenology hints at a subtle competition between orders—a mystery that must be unravelled to understand the proximate superconductor phase between $-3 \leqslant \nu \leqslant -2$.

Theoretically, ground-state studies of TBG have primarily taken a strong-coupling approach [16–19], wherein the small dispersion of the flat band is treated perturbatively on top of the Coulomb interaction. The resulting possible phases at $\nu = -3$ include quantum anomalous Hall (QAH) ferromagnets [18] and charge-density-wave insulators [20,21], which are supported numerically from self-consistent Hartree-Fock (SCHF) [21–26], density renormalization group (DMRG) [20] and exact diagonalization (ED) [27,28]. However, these approaches neglect a crucial facet of realistic TBG devices: heterostrain. Heterostrain [29–34] is a mismatch in the strains of the two graphene layers, with typical experimental values in the range 0.03–0.7% [35–39]. This seemingly insignificant amount of heterostrain amplifies the kinetic energy of the flat bands enormously, boosting their bandwidth to the same order as the interaction scale [Fig. 1(b)]. In this realistic intermediate coupling regime, a chief phase candidate is the "incommensurate Kekulé spiral" (IKS) phase, identified at mean-field level in [24,40].

Connecting these proposals to experiment requires an unbiased solution of the many-body problem at $\nu = -3$. SCHF, for instance, can be biased toward insulating states [41] (which could explain its failure to find metallic states at $|\nu| = 3$). On the other hand, the large number of degrees of freedom makes ED or DMRG computationally demanding. The largest ED on unstrained TBG has at most 3×3 unit cells at $|\nu| = 3$ when keeping valley and spin degrees of freedom. But such small systems may be biased when trying to capture an incommensurate state such as the IKS. Similarly, DMRG calculations performed on MATBG to date assume valley/spin polarization to reduce computational cost [20,31,42], excluding several promising ground state candidates. Quantum Monte Carlo suffers from a sign problem away from $\nu = 0$, making it impractical [43,44]. It is therefore imperative to perform full-scale DMRG studies with all flavors of electrons to resolve the competition among all ground state candidates.

In this work, we perform eight-flavor DMRG to establish the ground state phase diagram of TBG at $|\nu| = 3$ with heterostrain $\varepsilon_{\mathrm{Gr}}$. We find a phase diagram, summarized in Fig. 1(c), that unified all previous phase candidates. The key results are fourfold.

(i) The ground state at vanishing strain carries spin-polarized QAH order with intervalley coherence (QAH-IVC), which is nearly degenerate with the valley-polarized variant

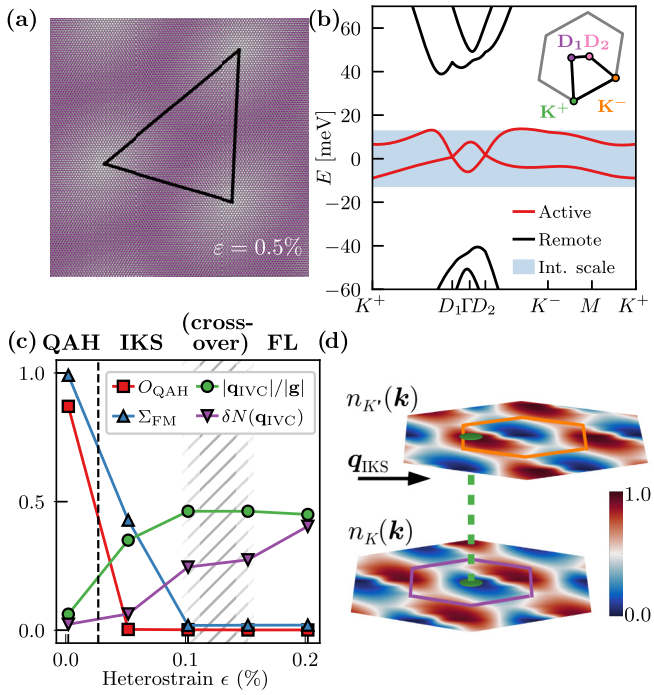

FIG. 1. (a) Moiré pattern from two graphene lattices with 1° relative twist and $\varepsilon_{\rm Gr} = 0.5\%$ uniaxial heterostrain. Strain is amplified at the superlattice scale, significantly distorting the moire unit cell. (b) Noninteracting bandstructure of TBG with $\varepsilon_{\rm Gr} = 0.3\%$ heterostrain. Heterostrain shifts the Dirac nodes $D_{1,2}$ close to the Γ point (inset). (c) Phase diagram of TBG at $|\nu| = 3$ obtained from DMRG up to bond dimension $\chi = 24\,576$. The phase transitions are identified with their characteristic order parameters: Chern band polarization $O_{\rm QAH}$, ferromagnetic order magnitude $\Sigma_{\rm FM}$, intervalley coherence wave vector $\boldsymbol{q}_{\rm IVC}$, and deviation of valley-summed electron density from uniform filling $\delta N(\boldsymbol{q}_{\rm IVC})$ (see main text for the definition). (d) Valley-nested DMRG electron occupations of the first Brillouin zone in the IKS phase (parameters match Fig. 2, $L_y = 6$). The relative shift $\boldsymbol{q}_{\rm IKS}$ makes the total occupations uniform while Γ is depleted in both valleys.

(QAH-VP) identified in past studies. We expect electron-phonon coupling (EPC) observed in recent experiments [45] to favor QAH-IVC.

(ii) Low strain stabilizes the spin-polarized IKS state, reinforcing the recent prediction from the mean-field study [24] to a much more robust level.

(iii) Intermediate strain drives a transition from flavor-polarized IKS to fully-symmetric Fermi liquid (FL), with close energy competition in their crossover region.

(iv) There is a large low-energy manifold of "Γ-depleted" orders—states where the electron occupation is low in the vicinity of the Γ point. The IKS phase is one such order, but others such as commensurate spin spirals (CSS) appear as close competitors.

Our study highlights the complex competition between a large manifold of distinct orders and selects the global ground state of TBG at $\nu = 3$ among various proposals. Equipped with this unbiased prediction from DMRG, we conclude with concrete near-term experiments that would confirm these predictions.

I. MODEL AND HETEROSTRAIN

We use a standard Bistrizer-MacDonald (BM) model [46] of TBG at twist angle $\theta = 1.08°$, and add realistic heterostrain [30] and strong Coulomb interactions. We take chiral ratio $\kappa = w_{\rm AA}/w_{\rm AB} = 0.65$, where $w_{\rm AA/AB}$ are interlayer tunneling strengths for different sublattices, in the realistic range 0.5–0.8 to account for some lattice relaxation [47–49]. Heterostrain modifies the Hamiltonian as an effective layer-dependent vector potential $-i\nabla \to -i\nabla + \boldsymbol{A}_\ell$ [30,47,50–59]:

$$\mathbf{A}_\ell = -\frac{\ell}{2}\frac{\beta\sqrt{3}}{2a}(\epsilon_{xx} - \epsilon_{yy}, -2\epsilon_{xy}), \tag{1}$$

and also distort lattice vectors $\boldsymbol{a}_i$ [and reciprocal vectors $\boldsymbol{g}_i$)] such that C_{3z} and C_{2x} are strongly broken, while C_{2z} and time-reversal are preserved [30].

Figure 1(b) shows the band structure for a single valley and spin in the presence of strain. Crucially, even subpercent level of heterostrain can dramatically increase the flat band dispersion of TBG as much as tenfold. The reason graphene-scale heterostrain $\varepsilon_{\rm Gr}$ has such a large effect is that the strain $\varepsilon_{\rm moiré}$ it produces on the moiré superlattice is amplified by a factor of inverse twist angle $1/\theta \sim 100$ (see Appendix B of the Supplemental Material [15]):

$$\varepsilon_{\rm moiré} \propto \frac{\varepsilon_{\rm Gr}}{\theta}. \tag{2}$$

Quantitatively, the narrow bands of TBG have bandwidth of 2.5 meV without heterostrain, which increases to 16 meV at $\varepsilon_{\rm Gr} = 0.2\%$ and 40 meV by $\varepsilon_{\rm Gr} = 0.5\%$—comparable to the Coulomb scale of 30–50meV. Heterostrain is therefore an experimental parameter of paramount importance to accurately determine the ground state phase diagram of TBG.

We consider interacting physics within the eight narrow ("flat") bands of TBG. A complete description of the model is given in Appendix C of the Supplemental Material [15]. We use a Chern or "maximally sublattice polarized" [18] basis $\hat{c}^\dagger_{\boldsymbol{k}\sigma\tau s}$ where $(\sigma, \tau, s) = (A/B, K/K', \uparrow/\downarrow)$ label sublattice, valley, and spin. These bands have Chern number $C = \sigma\tau$. Below we will use corresponding Pauli matrices σ^μ, τ^μ, and s^μ. The Hamiltonian is

$$\hat{H} = \sum_{\boldsymbol{k}} \hat{c}^\dagger_{\boldsymbol{k}} h_{\boldsymbol{k}} \hat{c}_{\boldsymbol{k}} + \frac{1}{2}\sum_{\boldsymbol{q}} V_{\boldsymbol{q}} : \hat{\rho}_{\boldsymbol{q}}\hat{\rho}_{-\boldsymbol{q}} :, \tag{3}$$

where $\hat{\rho}_{\boldsymbol{q}}$ is the (8×8 component) flat band density operator at momentum $\boldsymbol{q}$ and $V_{\boldsymbol{q}}$ is the double gate-screened Coulomb interaction, normal ordered relative to the background. As usual, the dispersion $h_{\boldsymbol{k}}$ is the BM part minus a correction to avoid double-counting Coulomb interactions [18,42]. The model studied here has approximate particle-hole symmetry [24], so ground states at $\nu = -3$ and 3 are nearly identical; we take $\nu = -3$.

Our DMRG calculations are performed on an infinite cylinder geometry with a circumference of L_y moiré unit cells. We choose a computational "cylinder" basis $\hat{c}_{n,k_y,\sigma\tau s}$ of hybrid Wannier orbitals that are maximally (exponentially) localized at the nth unit cell along the cylinder axis, but have definite

momentum k_y around the cylinder [20,42,60]. Fourier transformed, our model captures L_y line cuts through the moiré Brillouin zone at $k_y = \frac{2\pi m}{L_y}$, $-L_y \leqslant 2m < L_y$. The long-range interactions in the Hamiltonian, encoded as matrix product operators (MPO) in DMRG, are faithfully compressed [42,61] to accuracy $<10^{-2}$ meV at all distances. Our simulations required significant numerical resources. The $L_y = 4$ Hamiltonian has MPO bond dimension $\chi_{\text{MPO}} \approx 2000$, and we consider states up to bond dimension $\chi = 24\,576$. Our algorithm conserves electron occupation in each spin and valley $(U(1)_{\uparrow K} \times U(1)_{\downarrow K} \times U(1)_{\uparrow K'} \times U(1)_{\downarrow K'})$ as well as crystalline momentum along the circumference of the cylinder. We focus on the spin/valley unpolarized $(\tau^z, s^z) = (0, 0)$ sector with zero crystalline momentum. See Appendix D of the Supplemental Material [15] for details. Each unit cell on our cylinder consists of $L_y \times 8$ orbitals (already beyond normal exact diagonalization), and each datapoint requires $\sim 40\,000$ core hours.

II. VANISHING STRAIN: QAH-IVC ORDER

We start near zero strain, where strong coupling theories [18,19] predict a ground state with quantized anomalous Hall order. Previous numerical studies [21–28] have singled out QAH states with spin and valley polarization (QAH-VP), even when allowing $U_V(1)$ symmetry breaking. If we assume valley-polarization, DMRG recapitulates this finding. However, our treatment of all eight flavors allows us to drop this assumption. With total spin and valley charge zero, we find a new ground state candidate: a QAH insulator with intervalley coherent order (QAH-IVC). We briefly detail these states to introduce our method and notation, then consider larger strains.

QAH states have a time-reversal breaking order parameter

$$O_{\text{QAH}} = \frac{1}{N_k} \sum_{\boldsymbol{k}} \langle \hat{c}^\dagger_{\boldsymbol{k}} \sigma^z \tau^z \hat{c}_{\boldsymbol{k}} \rangle \tag{4}$$

that measures the polarization of the Chern bands. Despite their similar names, QAH-VP and QAH-IVC have unequal flavor polarizations, and hence, strikingly different charge density patterns at the graphene scale. These orders are adiabatically connected to "model" Slater determinant states specified by correlation matrices $P_{\alpha\beta}(\boldsymbol{k}) = \langle \hat{c}^\dagger_{\boldsymbol{k},\beta} \hat{c}_{\boldsymbol{k},\alpha} \rangle$. Explicitly, the "model" QAH-VP state at $\nu = -3$ has $O_{\text{QAH}} = 1$:

$$P_{\text{QAH-VP}}(\boldsymbol{k}) = \left(\frac{1+\sigma^z\tau^z}{2}\right)\left(\frac{1+\tau^z}{2}\right)\left(\frac{1+s^z}{2}\right), \tag{5}$$

with flavor polarization $(\tau^z, s^z) = (1, 1)$. By contrast, the "model" QAH-IVC state with spin along x is

$$P_{\text{QAH-IVC}} = \left(\frac{1+\sigma^z\tau^z}{2}\right)\left(\frac{1+\sigma^x\tau^x}{2}\right)\left(\frac{1+s^x}{2}\right), \tag{6}$$

with zero flavor polarization $(\tau^z, s^z) = (0, 0)$. This state also has $O_{\text{QAH}} = 1$.

Figure 1(c) shows O_{QAH} versus ε_{Gr} in the (0,0) sector. At $\varepsilon_{\text{Gr}} \approx 0$, we find $O_{\text{QAH}} \approx 0.87$ (slightly depolarized due to band hybridization), signaling QAH order before an abrupt transition at $\varepsilon_{\text{Gr}} \approx 0.05\%$. To confirm this as QAH-IVC order, we define intervalley coherent (IVC) and ferromagnetic (FM) order parameters (used repeatedly below):

$$\hat{\Delta}_{\text{IVC}} = \sum_{\boldsymbol{k}} \hat{c}^\dagger_{\boldsymbol{k}} \sigma^x \tau^+ \hat{c}_{\boldsymbol{k}}, \quad \hat{\Delta}_{\text{FM}} = \sum_{\boldsymbol{k}} \hat{c}^\dagger_{\boldsymbol{k}} s^+ \hat{c}_{\boldsymbol{k}}. \tag{7}$$

As these two-electron operators are off diagonal in the conserved quantities τ^z/s^z, they identically vanish; we must instead measure a four-electron correlator of their Fourier transform (Appendix D of the Supplemental Material [15] for details and the relation to Hohenberg-Mermin-Wagner theorem). Explicitly, for

$$\hat{\Delta}_{\text{FM}}(n) = \sum_{k_y} \hat{c}^\dagger_{n,k_y} s^+ \hat{c}_{n,k_y} \tag{8}$$

we consider

$$C_{\text{FM}}(n) = \langle \hat{\Delta}_{\text{FM}}(0) \hat{\Delta}^\dagger_{\text{FM}}(n) \rangle, \quad \Sigma_{\text{FM}} \equiv \sum_n |C_{\text{FM}}(n)|, \tag{9}$$

and define C_{IVC}, Σ_{IVC} analogously. Since $\Sigma_{\text{FM/IVC}}$ captures how fast $C_{\text{FM/IVC}}$ decays, a large $\Sigma_{\text{FM/IVC}}$ quantitatively distinguishes long-range FM/IVC ordering from other short-range phases with smaller $\Sigma_{\text{FM/IVC}}$. (We provide more precise distinctions in Appendixes E and G in the Supplemental Material).

Figure 1(c) shows $\Sigma_{\text{FM}} \approx 1$ at $\varepsilon_{\text{Gr}} = 0\%$ and we find Σ_{IVC} is also large, confirming QAH-IVC order in the $(\tau^z, s^z) = (0, 0)$ sector at vanishing strain. Appendix F1 in Supplemental Material [15] examines the valley-polarized sector (1,1), finding QAH-VP order. These two QAH states are nearly degenerate, with QAH-VP lower by 0.1 meV per electron at $\varepsilon_{\text{Gr}} = 0\%$—two orders of magnitude below the Coulomb scale. This near degeneracy is due to the proximity of our system to the "chiral limit" [62], where these QAH states are related by an emergent $U(4)_\pm$ symmetry [18]. Following the analysis of Ref. [63], the electron-phonon coupling will split the degeneracy in favor of the QAH-IVC state. Our results so far match strong coupling theory, but strains of only 0.05% change the picture entirely.

III. LOW STRAIN: IKS ORDER

At low strains $\varepsilon_{\text{Gr}} = 0.05 - 0.1\%$ we now show the ground state has an incommensurate valley spiral order and identify the phase as the *incommensurate* Kekulé spiral (IKS) [24]. Previous work on this phase was limited to mean-field level, leaving open the reasonable scenario that this incommensurate order is destroyed by strong fluctuations. Our key result here is that IKS is indeed stable to fluctuations—partially due to its "Γ-depletion" property, as we explain below—making it the many-body ground state at intermediate strain.

We briefly overview the IKS phase and then provide numerical results. IKS order breaks both moiré translation symmetry $\hat{T}_{\boldsymbol{a}_{1,2}}$ as well as $U(1)_{\text{valley}} = e^{i\theta_v \tau^z}$ symmetry down to a combined symmetry

$$\hat{T}^{\text{IKS}}_{\boldsymbol{a}_i} = \hat{T}_{\boldsymbol{a}_i} e^{i\boldsymbol{q}_{\text{IKS}} \cdot \boldsymbol{a}_i \tau^z/2}. \tag{10}$$

This produces an incommensurate real space spiral of the order parameter: $\theta_v(\boldsymbol{r} + \boldsymbol{a}_i) = \theta_v(\boldsymbol{r}) + \boldsymbol{a}_i \cdot \boldsymbol{q}_{\text{IKS}}$, observable in STM as a slowly changing Kekulé order between unit cells [39,64]. At $\nu = -3$, the IKS phase is an insulator with ferromagnetic and intervalley coherent order, similar to QAH-IVC.

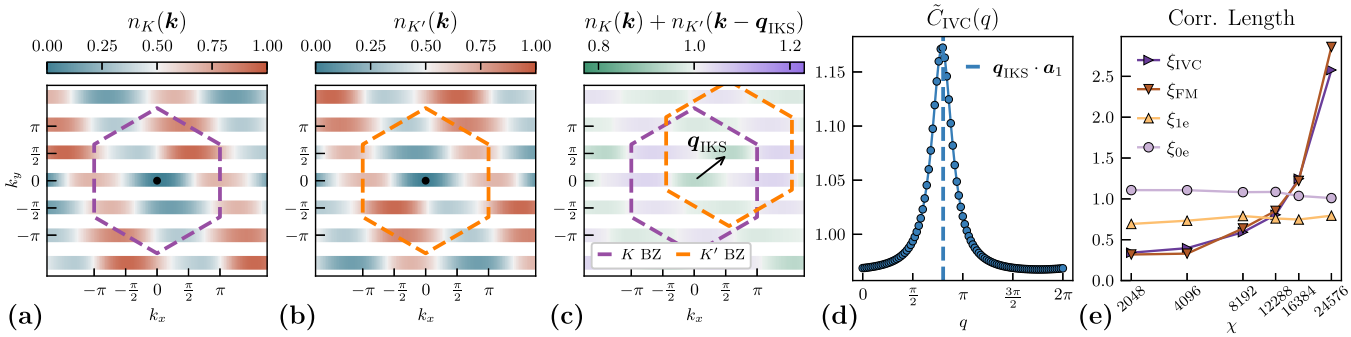

FIG. 2. IKS at $\varepsilon_{\rm Gr} = 0.05\%$. (a), (b) Valley-resolved electron density of TBG at $\nu = -3$. Dashed hexagons denote the first Brillouin zone, and the dot in the middle is the Γ point. (c) Total electron density $N_{\boldsymbol{q}_{\rm IKS}}(\boldsymbol{k})$ in Eq. (12), after a relative boost by $\boldsymbol{q}_{\rm IKS}$, whereupon the density becomes uniform. (d) Fourier transform of the IKS correlation function. The peak at $q \approx 0.80\pi$ matches $\boldsymbol{q}_{\rm IKS} \cdot \boldsymbol{a}_1$ from (c). (e) Scaling analysis of correlation lengths of several order parameters, showing that IVC and FM dominate at large bond dimensions $\chi > 16\,384$.

Unlike QAH-IVC, IKS order preserves time-reversal symmetry (so $O_{\rm QAH} = 0$) and has intervalley coherence only at wave vector $\boldsymbol{q}_{\rm IKS}$, condensing

$$\hat{\Delta}_{\rm IKS} = \sum_{\boldsymbol{k}} \hat{c}^\dagger_{\boldsymbol{k}+\boldsymbol{q}_{\rm IKS}} \sigma^x \tau^x \hat{c}_{\boldsymbol{k}}. \tag{11}$$

A "model" correlation matrix for IKS order must reflect $\hat{\Delta}_{\rm IKS}$ via coherence between the two valleys at $\boldsymbol{k}$ and $\boldsymbol{k} + \boldsymbol{q}_{\rm IKS}$.

We now show these distinctive features of IKS order in DMRG. Figures 2(a) and 2(b) shows the electron density $n_{\rm K/K'}(\boldsymbol{k})$ for each valley. The valleys are related by time-reversal symmetry $n_{\rm K}(\boldsymbol{k}) = n_{\rm K'}(-\boldsymbol{k})$. The region near Γ is depleted in both valleys; we comment below why this crucial feature minimizes the energy of IKS. Remarkably, a shift by $\boldsymbol{q}_{\rm IKS} = 0.40\boldsymbol{g}_1 + 0.25\boldsymbol{g}_2$ reveals a nearly uniform electron density as shown in Fig. 2(c):

$$N_{\boldsymbol{q}_{\rm IKS}}(\boldsymbol{k}) = n_{\rm K}(\boldsymbol{k}) + n_{\rm K'}(\boldsymbol{k} - \boldsymbol{q}_{\rm IKS}) \approx 1, \tag{12}$$

consistent with a "model" correlation matrix for the IKS insulator $P_{\rm IKS} \sim \langle \hat{c}^\dagger_{\boldsymbol{k}+\boldsymbol{q}_{\rm IKS}} \sigma^\mu \tau^x \hat{c}_{\boldsymbol{k}} \rangle$ with uniform filling. To examine this quantitatively, we compute $q_{\rm IVC}$ that minimizes

$$\delta N(\Delta\boldsymbol{q}) = \max_{\boldsymbol{k}} |n_{\rm K}(\boldsymbol{k}) + n_{\rm K'}(\boldsymbol{k} - \Delta\boldsymbol{q}) - 1| \tag{13}$$

and plot it in Fig. 1(c). We find δN is small while $|\boldsymbol{q}_{\rm IVC}|$ is large, consistent with IKS order.

Next, we directly analyze the IVC and FM orders within the IKS phase, providing another determination of $\boldsymbol{q}_{\rm IKS}$. Figure 1(c) shows FM order $\Sigma_{\rm FM}$ is the same order of magnitude as in the QAH-IVC phase. The IVC order, on the other hand, needs to be generalized with translation breaking to capture IKS:

$$\Delta_{\rm IKS}(n; q_y) = \sum_{k_y} \hat{c}^\dagger_{n,k_y+q_y} \sigma^x \tau^+ \hat{c}_{n,k_y}. \tag{14}$$

In this way, the corresponding correlator $C_{\rm IKS}(n; q_y)$ will show the phase spiral at wave vector $\boldsymbol{q}_{\rm IKS}$:

$$\mathrm{Arg}\big[C_{\rm IKS}\big(n; q_y = q^y_{\rm IKS}\big)\big] \sim (\boldsymbol{q}_{\rm IKS} \cdot \boldsymbol{a}_1) n. \tag{15}$$

In Fig. 2(d) we show the Fourier transform of $C_{\rm IKS}(n; q_y)$ with the expected $q^y_{\rm IKS} = 0.25|\boldsymbol{g}_2|$: $\tilde{C}_{\rm IKS}(q) = \mathcal{F}[C_{\rm IKS}(n; q^y_{\rm IKS})]$, which indeed exhibits a sharp peak at $q = \boldsymbol{q}_{\rm IKS} \cdot \boldsymbol{a}_1/2\pi \approx 0.40$. This suggests that $\boldsymbol{q}_{\rm IKS} = 0.40\boldsymbol{g}_1 + 0.25\boldsymbol{g}_2$, which is consistent with that determined from the electron occupation.

Finally, we establish (quasi-)long-range order corresponding to IVC and FM order parameters. To do so, we extract the correlation length $\xi_{\rm FM/IVC}$ from the long distance behavior of the correlator $|C_{\rm FM,IKS}(n)| \approx e^{-n/\xi_{\rm FM,IKS}}$. If the state has(quasi-)long-range order, ξ should diverge with the DMRG bond dimension χ. In Fig. 2(e), we plot the correlation length ξ corresponding to various operators, and observe that $\xi_{\rm FM/IKS}$ indeed sharply increases with χ. On the other hand, correlation lengths for operators with no long-range order, such as $\hat{\Delta}_{1e} \sim \hat{c}_{\boldsymbol{k}}$, $\hat{\Delta}_{0e} \sim \hat{c}^\dagger_{\boldsymbol{k}} \hat{c}_{\boldsymbol{k}'}$, do not increase with χ. We conclude that, even in the presence of fluctuations, the many-body ground state at low strains is the IKS phase.

IV. INTERMEDIATE STRAIN: FERMI LIQUID

At yet-higher strains, the increasingly large dispersion renders IKS less favorable than a conventional Fermi liquid (FL). The Fermi liquid is the "normal" state with a fully symmetric occupation in each valley and spin that partially fills the (interaction-renormalized) band structure. This is the state found in DMRG at $\varepsilon_{\rm Gr} = 0.2\%$. On the other hand, the ground states at lower strains show a "mixed" order with both metallic and flavor-polarized features, highlighting the close competition of different orders at the IKS-FL crossover region.

Figures 1(c) and 3 show the key features of the FL phase at $\varepsilon_{\rm Gr} = 0.2\%$. Unlike IKS, the electron density $n_{\rm K/K'}(\boldsymbol{k})$ shown in Figs. 3(a) and 3(b) is concentrated into a few small pockets that cannot be nested into close-to-uniform filling, with $\delta N(\mathbf{q}_0) \approx 0.4$ even at the minimizing wave vector $\mathbf{q}_0$. Moreover, these pockets are reminiscent of Fermi surfaces of metallic states, which closely match those obtained from symmetry-enforced SCHF as shown in Fig. 3(c). A closer look at momentum wire $k_y = \pi/2$ is displayed in Fig. 3(d): although no sharp Fermi surfaces are observed due to the quasi-1D geometry, the DMRG state does manifest drops/increases of $n(\boldsymbol{k})$ where the Fermi surfaces are expected from SCHF. $n(k) \neq 0, 1$ in DMRG are expected from a combination of finite bond dimension and nonunity quasiparticle weight. Finally, both IVC and FM orders are small in the ground state compared to the IKS phase, suggesting the

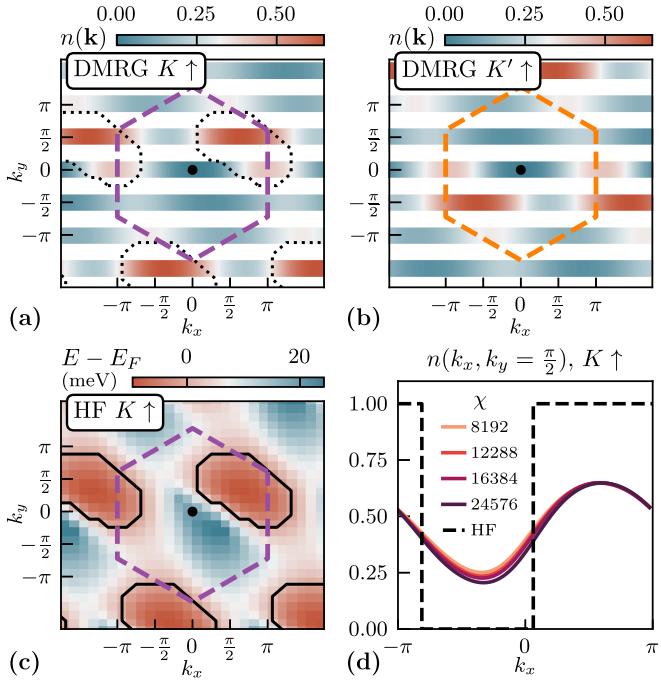

FIG. 3. FL at $\varepsilon_{\rm Gr} = 0.2\%$. (a), (b) Spin-up electron density in $K^{(\prime)}$ valley, plotted similarly to Fig. 2. The spin-down sector is related by the spin-flip symmetry s^x and shows identical occupations. Dotted lines in (a) circled the Fermi surfaces predicted from fully symmetric SCHF. (c) Energy $E(k)$ of the partially occupied band from SCHF. The electron only occupies the regions circled in solid lines, forming sharp Fermi surfaces. (d) The DMRG electron occupations in $(K, \uparrow)$ sector along the $k_y = \frac{\pi}{2}$ wire at various bond dimensions, where the filled/emptied regions closely matches that of SCHF (dashed lines).

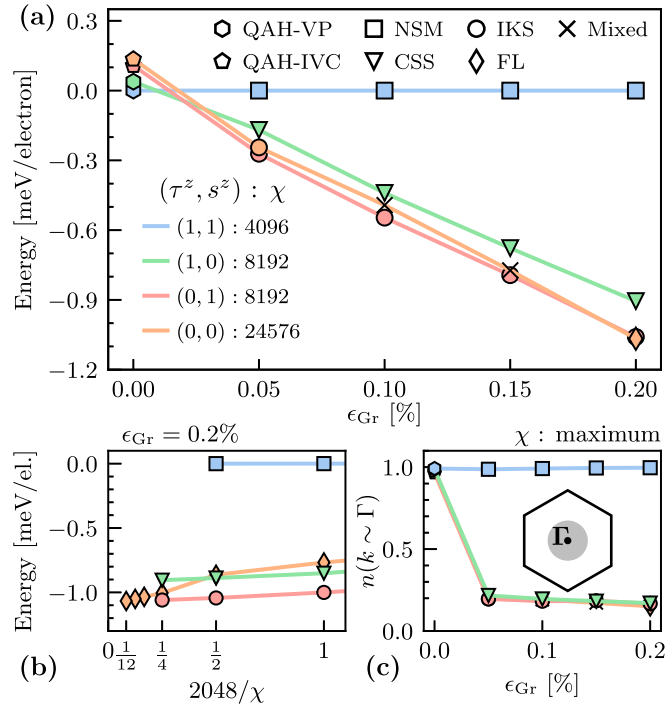

FIG. 4. (a) DMRG energies in all four sectors as a function of heterostrain $\varepsilon_{\rm Gr} \leqslant 0.2\%$. The (1,0) sector was not computed beyond $\varepsilon_{\rm Gr} = 0.2\%$, but is expected to be above (0,0) and (0,1) in energy. (b) The energy of different flavor sectors as a function of χ at $\varepsilon_{\rm Gr} = 0.2\%$. (c) Electron density per momentum near Γ: $n(k \sim \Gamma) = \sum_{|k|<1/5|g_1|} n(k)$. Parameters match Fig. 2.

absence of flavor order. Therefore, we conclude that $\nu = -3$ ground state at $\varepsilon_{\rm Gr} = 0.2\%$ is consistent with a symmetric Fermi liquid in 2D.

For $\varepsilon_{\rm Gr} = 0.1 - 0.15\%$ [Fig. 1(c), shaded region], DMRG is inconclusive about the nature of the state. These states exhibit features of both the FL state, such as large variations in $n(\boldsymbol{k})$, and small FM and IVC order. However, the state also shows a spin density wave not present in either the FL or IKS phases (Appendix G3 in the Supplemental Material [15]). We attribute this to the extremely close competition between FL and IKS here, not resolved at our largest bond dimensions.

V. STRAIN FAVORS Γ-DEPLETED STATES

A key conclusion from the previous section is the importance of the Γ point: away from zero strain, all DMRG ground states in (0,0) sector feature electron depletion at Γ point. The reason can be understood at the mean-field level even without symmetry breaking. The combination of the Hartree potential and strain-induced dispersion creates a sharp peak in the mean-field bandstructure, Fig. 3(c) (see also Appendix D in the Supplemental Material [15]). Therefore, any state that occupies this region incurs a substantial kinetic energy penalty, favoring Γ-depleted states. Below we show that this is in fact a general feature of ground-state competition of TBG: Γ-depleted states form a low-energy manifold, wherein an intricate competition picks out the true ground state.

In Fig. 4(a), we compare the ground state energy of DMRG ground state in (0, 0) sector to those in other (τ^z, s^z) sectors, which feature different ground-state orders under enforced flavor polarization (see Appendix F in the Supplemental Material [15] for their phase identification). At vanishing strain $\varepsilon_{\rm Gr}$, energy competition is tight between different sectors, as they all manifest QAH-VP or QAH-IVC. However, at larger strains there is a clear energy separation between (1, 1) sector and other sectors, which increases linearly with strain. This is explained by Fig. 4(c), where all low-energy states share the Γ-depleted feature. Meanwhile, the energy difference within the low-energy manifold is only around 0.3 meV, which is hardly resolved at the largest bond dimension [Fig. 4(b)]. We speculate that the difficulty of resolving the IKS to FL transition within DMRG is likely due to this proliferation of low-energy states.

VI. DISCUSSION AND IMPLICATIONS

Our realistic microscopic model, Eq. (3), has reasonably neglected a number of effects at the 0.1 meV level, such as intervalley scattering terms in the Coulomb interaction and anisotropy [18]. However, there are also a number of possible phenomena on the 1 meV scale that we have not yet included, such as lattice relaxation, particle-hole symmetry breaking [65], and, notably, the electron-phonon coupling (EPC) uncovered in recent studies [63]. Quantitatively determining the contribution of each perturbation is crucial to identify the

accurate phase diagram. For example, it is argued in Ref. [63] that EPC lowers the energy of intervalley orders by order of 0.5 meV, which clearly favors QAH-IVC and IKS over their competitive counterparts. This, in particular, suggests the Chern insulators found at finite magnetic field [66] may be connected to QAH-IVC. We leave the implementation of these perturbations to future work.

Experimentally, our results suggest that the amount of heterostrain present in virtually all experimental samples is more than sufficient to push TBG into the intermediate coupling regime. In this regime, our numerics suggest IKS as the primary insulating ground state candidate at $|\nu| = 3$, which is consistent with the great majority of experiments (see the Table in Appendix A in the Supplemental Material [15]) at $\nu = 3$. (We do note this is specific to samples not aligned to an hBN substrate; alignment strongly favors the QAH phase [67,68]). We also suggest FL as a competitive ground-state candidate at the intermediate-strain region, which might explain why most experiments find a metallic state near $\nu = -3$ (e.g., selected by particle-hole breaking effects). We also note that QAH-IVC might be identified in the rare ultralow strain samples [39].

The predicted phases at $|\nu| = 3$ could be directly confirmed by atomically resolved STM experiments [64,69]: the IVC order in QAH-IVC and IKS will result in charge density wave on the graphene lattice at "Kekulé" wave vector $\boldsymbol{Q} = \boldsymbol{K} - \boldsymbol{K}'$, and the phase spiral of IKS is reflected in the changing pattern of such charge density wave on the moiré lattice at wave vector $\boldsymbol{q}_{\mathrm{IKS}}$. We note that both of these phenomena have been successfully identified in recent STM experiments focusing on $|\nu| = 2$ [39], confirming the physical relevance of IKS order.

ACKNOWLEDGMENTS

We thank Patrick Ledwith, Ilya Esterlis, Eslam Khalaf, Ashvin Vishwanath, Yves Kwan, Glenn Wagner, Steve Simon and Siddharth Parameswaran for insightful discussions and collaborations on related works. This work was primarily funded by the U.S. Department of Energy, Office of Science, Office of Basic Energy Sciences, Materials Sciences and Engineering Division under Contract No. DE-AC02-05-CH11231 (Theory of Materials program KC2301). This research is funded in part by the Gordon and Betty Moore Foundation's EPiQS Initiative, Grant GBMF8683 to D.E.P. T.S. is supported by Masason foundation. N.B. is supported by a University Research Fellowship of the Royal Society. This research used resources of the National Energy Research Scientific Computing Center (NERSC), a U.S. Department of Energy Office of Science User Facility located at Lawrence Berkeley National Laboratory, operated under Contract No. DE-AC02-05CH11231 using NERSC award BES-ERCAP0020043 and BES-ERCAP0024721. This research used the Lawrencium computational cluster resource provided by the IT Division at the Lawrence Berkeley National Laboratory (Supported by the Director, Office of Science, Office of Basic Energy Sciences, of the U.S. Department of Energy under Contract No. DE-AC02-05CH11231).

[1] X. Lu, P. Stepanov, W. Yang, M. Xie, M. A. Aamir, I. Das, C. Urgell, K. Watanabe, T. Taniguchi, G. Zhang, A. Bachtold, A. H. MacDonald, and D. K. Efetov, Superconductors, orbital magnets and correlated states in magic-angle bilayer graphene, Nature (London) **574**, 653 (2019).

[2] P. Stepanov, I. Das, X. Lu, A. Fahimniya, K. Watanabe, T. Taniguchi, F. H. L. Koppens, J. Lischner, L. Levitov, and D. K. Efetov, Untying the insulating and superconducting orders in magic-angle graphene, Nature (London) **583**, 375 (2020).

[3] A. Jaoui, I. Das, G. Di Battista, J. Díez-Mérida, X. Lu, K. Watanabe, T. Taniguchi, H. Ishizuka, L. Levitov, and D. K. Efetov, Quantum critical behaviour in magic-angle twisted bilayer graphene, Nat. Phys. **18**, 633 (2022).

[4] P. Stepanov, M. Xie, T. Taniguchi, K. Watanabe, X. Lu, A. H. MacDonald, B. A. Bernevig, and D. K. Efetov, Competing zero-field chern insulators in superconducting twisted bilayer graphene, Phys. Rev. Lett. **127**, 197701 (2021).

[5] Y. Cao, V. Fatemi, A. Demir, S. Fang, S. L. Tomarken, J. Y. Luo, J. D. Sanchez-Yamagishi, K. Watanabe, T. Taniguchi, E. Kaxiras, R. C. Ashoori, and P. Jarillo-Herrero, Correlated insulator behaviour at half-filling in magic-angle graphene superlattices, Nature (London) **556**, 80 (2018).

[6] U. Zondiner, A. Rozen, D. Rodan-Legrain, Y. Cao, R. Queiroz, T. Taniguchi, K. Watanabe, Y. Oreg, F. von Oppen, A. Stern, E. Berg, P. Jarillo-Herrero, and S. Ilani, Cascade of phase transitions and Dirac revivals in magic-angle graphene, Nature (London) **582**, 203 (2020).

[7] J. M. Park, Y. Cao, K. Watanabe, T. Taniguchi, and P. Jarillo-Herrero, Flavour Hund's coupling, Chern gaps and charge diffusivity in moiré graphene, Nature (London) **592**, 43 (2021).

[8] Y. Cao, D. Rodan-Legrain, J. M. Park, N. F. Q. Yuan, K. Watanabe, T. Taniguchi, R. M. Fernandes, L. Fu, and P. Jarillo-Herrero, Nematicity and competing orders in superconducting magic-angle graphene, Science **372**, 264 (2021).

[9] M. Yankowitz, S. Chen, H. Polshyn, Y. Zhang, K. Watanabe, T. Taniguchi, D. Graf, A. F. Young, and C. R. Dean, Tuning superconductivity in twisted bilayer graphene, Science **363**, 1059 (2019).

[10] Y. Saito, J. Ge, K. Watanabe, T. Taniguchi, and A. F. Young, Independent superconductors and correlated insulators in twisted bilayer graphene, Nat. Phys. **16**, 926 (2020).

[11] D. Wong, K. P. Nuckolls, M. Oh, B. Lian, Y. Xie, S. Jeon, K. Watanabe, T. Taniguchi, B. A. Bernevig, and A. Yazdani, Cascade of electronic transitions in magic-angle twisted bilayer graphene, Nature (London) **582**, 198 (2020).

[12] M. Oh, K. P. Nuckolls, D. Wong, R. L. Lee, X. Liu, K. Watanabe, T. Taniguchi, and A. Yazdani, Evidence for unconventional superconductivity in twisted bilayer graphene, Nature (London) **600**, 240 (2021).

[13] Y. Choi, H. Kim, C. Lewandowski, Y. Peng, A. Thomson, R. Polski, Y. Zhang, K. Watanabe, T. Taniguchi, J. Alicea, and S. Nadj-Perge, Interaction-driven band flattening and correlated phases in twisted bilayer graphene, Nat. Phys. **17**, 1375 (2021).

[14] J. Yu, B. A. Foutty, Z. Han, M. E. Barber, Y. Schattner, K. Watanabe, T. Taniguchi, P. Phillips, Z.-X. Shen, S. A. Kivelson, and B. E. Feldman, Correlated Hofstadter spectrum and flavour phase diagram in magic-angle twisted bilayer graphene, Nat. Phys. **18**, 825 (2022).

[15] See Supplemental Material at http://link.aps.org/supplemental/10.1103/PhysRevB.108.235128 for Appendixes A–G, which also includes Refs. [70–79].

[16] J. Kang and O. Vafek, Strong coupling phases of partially filled twisted bilayer graphene narrow bands, Phys. Rev. Lett. **122**, 246401 (2019).

[17] K. Seo, V. N. Kotov, and B. Uchoa, Ferromagnetic mott state in twisted graphene bilayers at the magic angle, Phys. Rev. Lett. **122**, 246402 (2019).

[18] N. Bultinck, E. Khalaf, S. Liu, S. Chatterjee, A. Vishwanath, and M. P. Zaletel, Ground state and hidden symmetry of magic-angle graphene at even integer filling, Phys. Rev. X **10**, 031034 (2020).

[19] B. Lian, Z.-D. Song, N. Regnault, D. K. Efetov, A. Yazdani, and B. A. Bernevig, Twisted bilayer graphene. IV. Exact insulator ground states and phase diagram, Phys. Rev. B **103**, 205414 (2021).

[20] J. Kang and O. Vafek, Non-Abelian Dirac node braiding and near-degeneracy of correlated phases at odd integer filling in magic-angle twisted bilayer graphene, Phys. Rev. B **102**, 035161 (2020).

[21] F. Xie, J. Kang, B. A. Bernevig, O. Vafek, and N. Regnault, Phase diagram of twisted bilayer graphene at filling factor $\nu=\pm 3$, Phys. Rev. B **107**, 075156 (2023).

[22] Y. Zhang, K. Jiang, Z. Wang, and F. Zhang, Correlated insulating phases of twisted bilayer graphene at commensurate filling fractions: A Hartree-Fock study, Phys. Rev. B **102**, 035136 (2020).

[23] M. Xie and A. H. MacDonald, Nature of the correlated insulator states in twisted bilayer graphene, Phys. Rev. Lett. **124**, 097601 (2020).

[24] Y. H. Kwan, G. Wagner, T. Soejima, M. P. Zaletel, S. H. Simon, S. A. Parameswaran, and N. Bultinck, Kekul'e spiral order at all nonzero integer fillings in twisted bilayer graphene, Phys. Rev. X **11**, 041063 (2021).

[25] J. Liu and X. Dai, Theories for the correlated insulating states and quantum anomalous Hall effect phenomena in twisted bilayer graphene, Phys. Rev. B **103**, 035427 (2021).

[26] K. Hejazi, X. Chen, and L. Balents, Hybrid Wannier Chern bands in magic angle twisted bilayer graphene and the quantized anomalous Hall effect, Phys. Rev. Res. **3**, 013242 (2021).

[27] P. Potasz, M. Xie, and A. H. MacDonald, Exact diagonalization for magic-angle twisted bilayer graphene, Phys. Rev. Lett. **127**, 147203 (2021).

[28] F. Xie, A. Cowsik, Z.-D. Song, B. Lian, B. A. Bernevig, and N. Regnault, Twisted bilayer graphene. VI. An exact diagonalization study at nonzero integer filling, Phys. Rev. B **103**, 205416 (2021).

[29] L. Huder, A. Artaud, T. Le Quang, G. T. de Laissardière, A. G. M. Jansen, G. Lapertot, C. Chapelier, and V. T. Renard, Electronic spectrum of twisted graphene layers under heterostrain, Phys. Rev. Lett. **120**, 156405 (2018).

[30] Z. Bi, N. F. Q. Yuan, and L. Fu, Designing flat bands by strain, Phys. Rev. B **100**, 035448 (2019).

[31] D. E. Parker, T. Soejima, J. Hauschild, M. P. Zaletel, and N. Bultinck, Strain-induced quantum phase transitions in magic-angle graphene, Phys. Rev. Lett. **127**, 027601 (2021).

[32] F. Mesple, A. Missaoui, T. Cea, L. Huder, F. Guinea, G. Trambly de Laissardière, C. Chapelier, and V. T. Renard, Heterostrain determines flat bands in magic-angle twisted graphene layers, Phys. Rev. Lett. **127**, 126405 (2021).

[33] Z.-B. Dai, Y. He, and Z. Li, Effects of heterostrain and lattice relaxation on the optical conductivity of twisted bilayer graphene, Phys. Rev. B **104**, 045403 (2021).

[34] X. Wang, J. Finney, A. L. Sharpe, L. K. Rodenbach, C. L. Hsueh, K. Watanabe, T. Taniguchi, M. A. Kastner, O. Vafek, and D. Goldhaber-Gordon, Unusual magnetotransport in twisted bilayer graphene from strain-induced open Fermi surfaces, Proc. Natl. Acad. Sci. USA **120**, e2307151120 (2023).

[35] A. Kerelsky, L. J. McGilly, D. M. Kennes, L. Xian, M. Yankowitz, S. Chen, K. Watanabe, T. Taniguchi, J. Hone, C. Dean, A. Rubio, and A. N. Pasupathy, Maximized electron interactions at the magic angle in twisted bilayer graphene, Nature (London) **572**, 95 (2019).

[36] Y. Choi, J. Kemmer, Y. Peng, A. Thomson, H. Arora, R. Polski, Y. Zhang, H. Ren, J. Alicea, G. Refael, F. von Oppen, K. Watanabe, T. Taniguchi, and S. Nadj-Perge, Electronic correlations in twisted bilayer graphene near the magic angle, Nat. Phys. **15**, 1174 (2019).

[37] Y. Xie, B. Lian, B. Jäck, X. Liu, C.-L. Chiu, K. Watanabe, T. Taniguchi, B. A. Bernevig, and A. Yazdani, Spectroscopic signatures of many-body correlations in magic-angle twisted bilayer graphene, Nature (London) **572**, 101 (2019).

[38] N. P. Kazmierczak, M. Van Winkle, C. Ophus, K. C. Bustillo, S. Carr, H. G. Brown, J. Ciston, T. Taniguchi, K. Watanabe, and D. K. Bediako, Strain fields in twisted bilayer graphene, Nat. Mater. **20**, 956 (2021).

[39] K. P. Nuckolls, R. L. Lee, M. Oh, D. Wong, T. Soejima, J. P. Hong, D. Călugăru, J. Herzog-Arbeitman, B. A. Bernevig, K. Watanabe, T. Taniguchi, N. Regnault, M. P. Zaletel, and A. Yazdani, Quantum textures of the many-body wavefunctions in magic-angle graphene, Nature (London) **620**, 525 (2023).

[40] G. Wagner, Y. H. Kwan, N. Bultinck, S. H. Simon, and S. A. Parameswaran, Global phase diagram of the normal state of twisted bilayer graphene, Phys. Rev. Lett. **128**, 156401 (2022).

[41] P. Mori-Sánchez, A. J. Cohen, and W. Yang, Localization and delocalization errors in density functional theory and implications for band-gap prediction, Phys. Rev. Lett. **100**, 146401 (2008).

[42] T. Soejima, D. E. Parker, N. Bultinck, J. Hauschild, and M. P. Zaletel, Efficient simulation of moiré materials using the density matrix renormalization group, Phys. Rev. B **102**, 205111 (2020).

[43] J. S. Hofmann, E. Khalaf, A. Vishwanath, E. Berg, and J. Y. Lee, Fermionic monte carlo study of a realistic model of twisted bilayer graphene, Phys. Rev. X **12**, 011061 (2022).

[44] X. Zhang, G. Pan, B.-B. Chen, H. Li, K. Sun, and Z. Y. Meng, Polynomial sign problem and topological mott insulator in twisted bilayer graphene, Phys. Rev. B **107**, L241105 (2023).

[45] C. Chen, K. P. Nuckolls, S. Ding, W. Miao, D. Wong, M. Oh, R. L. Lee, S. He, C. Peng, D. Pei, Y. Li, S. Zhang, J. Liu, Z. Liu, C. Jozwiak, A. Bostwick, E. Rotenberg, C. Li, X. Han, D. Pan *et al.*, Strong inter-valley electron-phonon coupling in magic-angle twisted bilayer graphene, arXiv:2303.14903.

[46] R. Bistritzer and A. H. MacDonald, Moiré bands in twisted double-layer graphene, Proc. Natl. Acad. Sci. **108**, 12233 (2011).
[47] N. N. T. Nam and M. Koshino, Lattice relaxation and energy band modulation in twisted bilayer graphene, Phys. Rev. B **96**, 075311 (2017).
[48] S. Carr, S. Fang, Z. Zhu, and E. Kaxiras, Exact continuum model for low-energy electronic states of twisted bilayer graphene, Phys. Rev. Res. **1**, 013001 (2019).
[49] P. J. Ledwith, E. Khalaf, Z. Zhu, S. Carr, E. Kaxiras, and A. Vishwanath, Tb or not tb? contrasting properties of twisted bilayer graphene and the alternating twist n-layer structures ($n = 3, 4, 5, \ldots$), arXiv:2111.11060.
[50] H. Suzuura and T. Ando, Phonons and electron-phonon scattering in carbon nanotubes, Phys. Rev. B **65**, 235412 (2002).
[51] J. L. Manes, Symmetry-based approach to electron-phonon interactions in graphene, Phys. Rev. B **76**, 045430 (2007).
[52] E.-A. Kim and A. H. Castro Neto, Graphene as an electronic membrane, EPL (Europhysics Letters) **84**, 57007 (2008).
[53] F. Guinea, B. Horovitz, and P. Le Doussal, Gauge field induced by ripples in graphene, Phys. Rev. B **77**, 205421 (2008).
[54] V. M. Pereira and A. H. Castro Neto, Strain engineering of graphene's electronic structure, Phys. Rev. Lett. **103**, 046801 (2009).
[55] M. A. H. Vozmediano, M. I. Katsnelson, and F. Guinea, Gauge fields in graphene, Phys. Rep. **496**, 109 (2010).
[56] F. de Juan, M. Sturla, and M. A. H. Vozmediano, Space dependent fermi velocity in strained graphene, Phys. Rev. Lett. **108**, 227205 (2012).
[57] J. L. Manes, F. de Juan, M. Sturla, and M. A. H. Vozmediano, Generalized effective hamiltonian for graphene under nonuniform strain, Phys. Rev. B **88**, 155405 (2013).
[58] F. de Juan, J. L. Manes, and M. A. H. Vozmediano, Gauge fields from strain in graphene, Phys. Rev. B **87**, 165131 (2013).
[59] M. Koshino and N. N. T. Nam, Effective continuum model for relaxed twisted bilayer graphene and moiré electron-phonon interaction, Phys. Rev. B **101**, 195425 (2020).
[60] J. Motruk, M. P. Zaletel, R. S. K. Mong, and F. Pollmann, Density matrix renormalization group on a cylinder in mixed real and momentum space, Phys. Rev. B **93**, 155139 (2016).
[61] D. E. Parker, X. Cao, and M. P. Zaletel, Local matrix product operators: Canonical form, compression, and control theory, Phys. Rev. B **102**, 035147 (2020).
[62] G. Tarnopolsky, A. J. Kruchkov, and A. Vishwanath, Origin of magic angles in twisted bilayer graphene, Phys. Rev. Lett. **122**, 106405 (2019).
[63] Y. H. Kwan, G. Wagner, N. Bultinck, S. H. Simon, E. Berg, and S. A. Parameswaran, Electron-phonon coupling and competing Kekul'e orders in twisted bilayer graphene, arXiv:2303.13602.
[64] J. P. Hong, T. Soejima, and M. P. Zaletel, Detecting symmetry breaking in magic angle graphene using scanning tunneling microscopy, Phys. Rev. Lett. **129**, 147001 (2022).
[65] J. Kang and O. Vafek, Pseudomagnetic fields, particle-hole asymmetry, and microscopic effective continuum Hamiltonians of twisted bilayer graphene, Phys. Rev. B **107**, 075408 (2023).
[66] K. P. Nuckolls, M. Oh, D. Wong, B. Lian, K. Watanabe, T. Taniguchi, B. A. Bernevig, and A. Yazdani, Strongly correlated Chern insulators in magic-angle twisted bilayer graphene, Nature (London) **588**, 610 (2020).
[67] A. L. Sharpe, E. J. Fox, A. W. Barnard, J. Finney, K. Watanabe, T. Taniguchi, M. A. Kastner, and D. Goldhaber-Gordon, Evidence of orbital ferromagnetism in twisted bilayer graphene aligned to hexagonal boron nitride, Nano Lett. **21**, 4299 (2021).
[68] M. Serlin, C. L. Tschirhart, H. Polshyn, Y. Zhang, J. Zhu, K. Watanabe, T. Taniguchi, L. Balents, and A. F. Young, Intrinsic quantized anomalous hall effect in a moiré heterostructure, Science **367**, 900 (2020).
[69] D. Călugăru, N. Regnault, M. Oh, K. P. Nuckolls, D. Wong, R. L. Lee, A. Yazdani, O. Vafek, and B. A. Bernevig, Spectroscopy of twisted bilayer graphene correlated insulators, Phys. Rev. Lett. **129**, 117602 (2022).
[70] Y. Saito, J. Ge, L. Rademaker, K. Watanabe, T. Taniguchi, D. A. Abanin, and A. F. Young, Hofstadter subband ferromagnetism and symmetry-broken Chern insulators in twisted bilayer graphene, Nat. Phys. **17**, 478 (2021).
[71] J. M. B. Lopes Dos Santos, N. M. R. Peres, and A. H. Castro Neto, Graphene bilayer with a twist: Electronic structure, Phys. Rev. Lett. **99**, 256802 (2007).
[72] D. Parker, P. Ledwith, E. Khalaf, T. Soejima, J. Hauschild, Y. Xie, A. Pierce, M. P. Zaletel, A. Yacoby, and A. Vishwanath, Field-tuned and zero-field fractional chern insulators in magic angle graphene, arXiv:2112.13837.
[73] O. Vafek and J. Kang, Renormalization group study of hidden symmetry in twisted bilayer graphene with coulomb interactions, Phys. Rev. Lett. **125**, 257602 (2020).
[74] M. Xie and A. H. MacDonald, Weak-field hall resistivity and spin-valley flavor symmetry breaking in magic-angle twisted bilayer graphene, Phys. Rev. Lett. **127**, 196401 (2021).
[75] B. Vanhecke, J. Haegeman, K. Van Acoleyen, L. Vanderstraeten, and F. Verstraete, Scaling hypothesis for matrix product states, Phys. Rev. Lett. **123**, 250604 (2019).
[76] E. Fradkin, *Field Theories of Condensed Matter Physics* (Cambridge University Press, Cambridge, England, 2013).
[77] S. Liu, E. Khalaf, J. Y. Lee, and A. Vishwanath, Nematic topological semimetal and insulator in magic-angle bilayer graphene at charge neutrality, Phys. Rev. Res. **3**, 013033 (2021).
[78] E. Khalaf, N. Bultinck, A. Vishwanath, and M. P. Zaletel, Soft modes in magic angle twisted bilayer graphene, arXiv:2009.14827.
[79] F. Pollmann, S. Mukerjee, A. M. Turner, and J. E. Moore, Theory of finite-entanglement scaling at one-dimensional quantum critical points, Phys. Rev. Lett. **102**, 255701 (2009).